

NOTES AND CORRESPONDENCE

On the Interannual Variability of the Indonesian Throughflow and Its Linkage with ENSO

MATTHEW H. ENGLAND

Centre for Environmental Modelling and Prediction, School of Mathematics, University of New South Wales, Sydney, New South Wales, Australia

FEI HUANG

Laboratory of Physical Oceanography, Ocean University of China, Qingdao, China, and University of New South Wales, Sydney, New South Wales, Australia

(Manuscript received 28 July 2003, in final form 28 July 2004)

ABSTRACT

The Indonesian Throughflow (ITF) variability is assessed using a retrospective analysis of the global ocean based on the Simple Ocean Data Assimilation (SODA) experiment spanning the period 1950–99. A comparison between the 1983–95 observed ITF, and the simulated ITF suggests a reasonably accurate reconstruction of ocean circulation in the vicinity of the ITF during the available measurement record. A wavelet analysis shows that once the seasonal cycle is removed, the dominant variation of the ITF anomaly is an interannual oscillation with a period of about 4–7 yr. This interannual variability is significantly correlated with the El Niño–Southern Oscillation (ENSO) pattern, with the ITF lagging the ENSO cycle by 8–9 months. This suggests that large-scale tropical ocean–atmosphere interaction plays an important role in the interannual variability of the ITF. Regional upper-ocean heat content variability might also play a role in controlling interannual fluctuations of the ITF transport via geostrophic flows, though it could equally be ITF variations that establish heat content anomalies downstream of the Indonesian archipelago. The model heat transport associated with the ITF is in good agreement with the limited observational record available. Resultant variability in annual mean ITF heat transport is in the range 0.4–1.2 PW, which is significantly correlated with ITF and ENSO indices.

1. Introduction

The Indonesian Throughflow (ITF) has long been a focus of research for its impact on local, regional, and global ocean circulation. At the large scale, it is one of the chokepoints of the global circulation system (Gordon 2001), and its variability is believed to affect climate on interannual and longer time scales (Wajsowicz and Schneider 2001; Schott and McCreary 2001). Observational studies have suggested the ITF transport oscillates in phase with ENSO: namely, larger ITF transport during La Niña conditions, and smaller ITF transport during El Niño phases (Bray et al. 1996; Fieuz et al. 1996; Gordon and Fine 1996; Meyers 1996; Gordon and McClean 1999). The new Arlindo current mooring observations within the Makassar Strait during

1996–98 have provided additional insight into throughflow variability, with the measurement period including the large 1997/98 ENSO event (Gordon and Susanto 1999). A correlation coefficient of 0.73 between Makassar transport and Southern Oscillation index (SOI) was found, though the time series is too short to assert a robust relationship between the ITF and ENSO.

Although many of the above-mentioned studies have found a linkage between the ITF and the ENSO cycle, the only observational analysis of a continuous decade-long time series is that of Meyers (1996). He found that the ITF transport was at a maximum during La Niña and weakened during El Niño, with a peak-to-peak amplitude of about 5 Sv ($1 \text{ Sv} = 10^6 \text{ m}^3 \text{ s}^{-1}$). However, the observations of the ITF transport run from May 1983 to November 1994, including only one La Niña (1988/89) and two El Niño events (1986/87, 1991/93) (adopting the definition of El Niño and La Niña events after Angell (1981) and Rasmusson and Carpenter (1982)). This is insufficient to confirm a relationship between the ITF and ENSO. For further analysis of the Meyers

Corresponding author address: Matthew H. England, Centre for Environmental Modelling and Prediction, School of Mathematics, University of New South Wales, Sydney, NSW, 2052, Australia.
E-mail: M.England@unsw.edu.au

(1996) record, we compare the time series of the ITF anomaly and the multivariate ENSO index (MEI; Wolter 1987; Wolter and Timlin 1993) month by month in Fig. 1a. Here we show the ITF anomaly about its long-term mean. We find a negative correlation (-0.27) between the ITF and ENSO, which is statistically significant at the 95% confidence level. Lag correlation analysis shows a maximum lagged coefficient of -0.35 with the ITF lagging the MEI by 8 months. This result mostly reflects the connection between the ITF anomaly and MEI during the 1988/89 La Niña phase. The ITF transport from the Pacific to Indian Ocean is anomalously strong during 1988/89, but its peak lags the cold phase by several months. With one dominant event during 1988/89, the observational record is perhaps too short to make conclusive statements about the role of Pacific Ocean variability in controlling ITF transport.

The goal of the present study is to examine the connection of the ITF to ENSO by analyzing a 50-yr reconstruction of ocean circulation in a global ocean data assimilation experiment. Several model studies have assessed the role of the ITF on the mean global ocean circulation (Hirst and Godfrey 1993; England 1993; Schiller et al. 1998; Kindle et al. 1989). Estimates of ITF strength have also been made using an ocean GCM forced by reanalysis winds during 1987–95 (Maltrud et al. 1998; Potemra et al. 1997) and the ITF was found to correlate negatively with ENSO. However, like the Meyers (1996) analysis, this period is dominated by the prominent cold ENSO phase during 1988/89. A longer simulation period (1981–97) is examined by Lee et al. (2002), who also note a link between ITF and ENSO (see their Fig. 6b). While not mentioned in their study, there is an apparent 6–9-month lag in the ITF phase compared with the Niño-3 and Niño-4 SST indices for some parts of the 1981–97 reconstruction. We aim to investigate the ITF–ENSO relationship using a longer model reconstruction record (1950–99) than previously analyzed. It will be some time, perhaps several decades, before interannual–decadal ITF variability can be estimated directly from ocean observations.

The rest of this note is organized as follows. In section 2 the datasets and analysis techniques are described, including an assessment of the ITF pathways and properties in the global ocean data assimilation experiment, which are compared to observations where available. Results are presented in section 3 and concluding remarks follow in section 4.

2. Data products and model assessment

a. Global ocean data assimilation model

The primary database for this study consists of monthly horizontal velocity fields and sea surface temperature (SST) from a retrospective analysis of the global ocean based on the Simple Ocean Data Assimilation (SODA version 7) package of Carton et al.

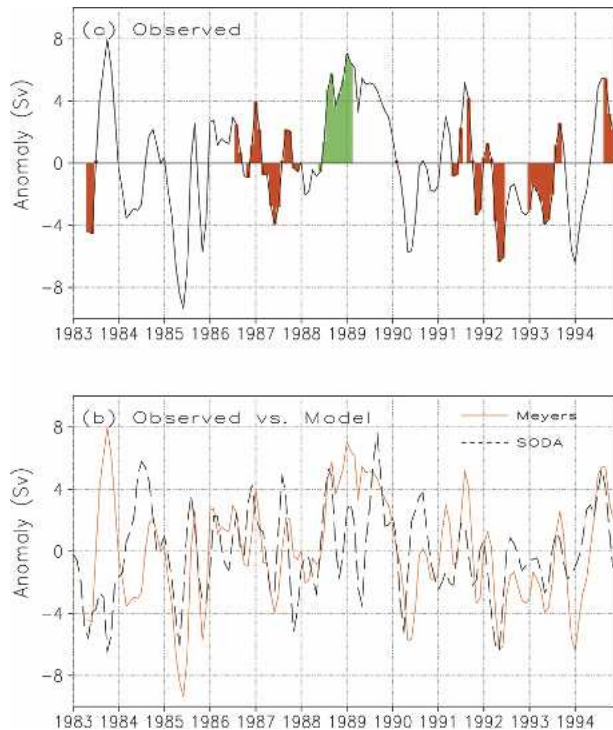


FIG. 1. (a) Time series of upper-ocean geostrophic transport anomaly (Sv) relative to 400 db during 1983–94 as estimated by Meyers (1996). The anomaly is calculated about the long-term mean of 5 Sv during 1983–94. Positive values indicate enhanced Pacific–Indian Ocean throughflow. The red and green bars show the warm and cold phases, respectively, of the ENSO cycle during 1983–94, based on the MEI obtained from the NOAA–CIRES Climate Diagnostics Center (CDC). (b) Comparison between the observed upper-ocean geostrophic transport anomaly (Sv) in (a) and that simulated in the SODA model (relative to 444 db). See text for the calculation details of the observed and modeled transport estimates.

(2000a,b). The SODA analysis takes all available observations and assimilates them using multivariate optimal interpolation into a global configuration of the second Geophysical Fluid Dynamics Laboratory (GFDL) Modular Ocean Model (MOM2) driven by the Comprehensive Ocean–Atmosphere Data Set (COADS) and the National Centers for Environmental Prediction (NCEP) winds. Assimilated data include subsurface temperature and salinity from the National Oceanographic Data Center (NODC) 1994 *World Ocean Atlas*, additional conductivity–temperature–depth (CTD) and expendable bathythermograph (XBT) data from the Global Temperature–Salinity Profile Project and other sources, thermistor temperature from the Tropical Atmosphere Ocean (TAO) array, in situ and satellite SST, and finally, satellite altimeter sea level data from *Geosat*, the *Earth Remote Sensing* satellites *ERS-1* and *ERS-2*, and *TOPEX/Poseidon*. The SODA data used in our study is monthly and spans the period 1950–99 inclusive, with a longitudinal resolution of 1.0° , a latitudinal resolution that varies gradually

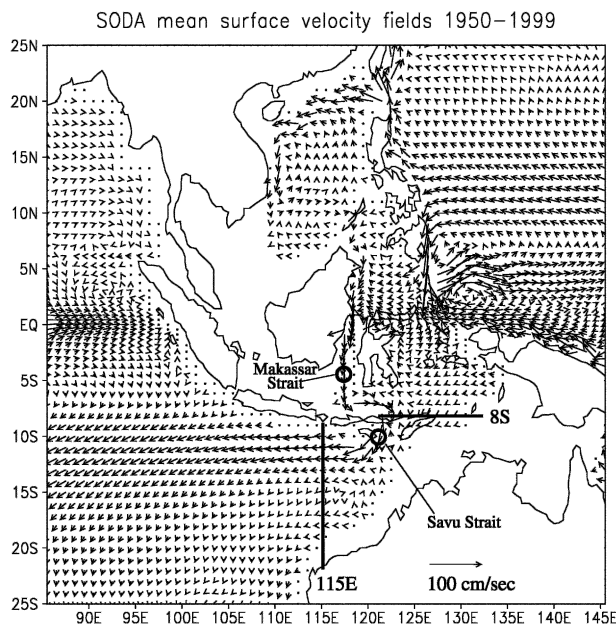


FIG. 2. Long-term mean SODA surface velocity vectors (cm s^{-1}) in the vicinity of Indonesia. Realistic landmass outlines are shown to highlight the simplification of model geometry in the Indonesian Archipelago. For example, the model has closed Lombok and Sumba Straits, and the Islands of Flores and Timor are submerged. This yields a single throughflow via a merged chokepoint covering Savu and Dao Straits and the Timor Passage. Also indicated are the locations of the 8°S , 115°E sections used to compute the ITF in Fig. 5, as well as the station locations in the Makassar Strait and the Savu Strait–Timor Passage used to plot $T - S$ and meridional velocity in Figs. 3 and 4.

from 0.43° at the equator to 1.02° at about 60°S and 60°N , and 20 levels in the vertical. It is noted that at this coarse resolution the SODA model can only be expected to agree with observed ITF transports and properties over spatial scales of the order or in excess of hundreds of kilometers laterally and $\approx 20\text{--}100$ m vertically.

b. Validation—Mean ITF properties

Before commencing an analysis of the ITF–ENSO link in the 50-yr global ocean data assimilation experiment, it is important to compare the SODA model with observations of ITF transport properties. In this subsection we consider the mean flow pathways and temperature – salinity ($T - S$) properties of the simulated ITF, comparing to observations where available. Figure 2 shows the long-term mean SODA surface velocity vector fields in the vicinity of Indonesia. Immediately obvious is the crude representation of the Indonesian Archipelago in the model, with no resolution of the Lombok or Sumba Straits, and the Islands of Flores and Timor submerged. This means the ITF flows via a broad model chokepoint that is in effect a merger of the Savu and Dao Straits with the Timor Passage. Much of the ITF appears at the western boundary of this channel; the model equivalent of Savu Strait. Farther up-

stream, the model ITF flows virtually exclusively via the Makassar Strait. At the surface, there is a weak mean northward flow to the east of Sulawesi in the Molucca Sea. Flow in the interior shows only weak bands of southward and northward flow in the Molucca Sea (not shown), and an enhanced jet of southward flow in the thermocline in the Makassar Strait (discussed below). The preference for the ITF to flow via the Makassar Strait is in good agreement with observations. Gordon et al. (1999) note that the observed flow through Makassar Strait is sufficient to account for all of the Pacific–Indian interocean transport.

Profiles of thermohaline properties in the SODA model also show good overall agreement with observations in the ITF region. Given the flow pathways noted above, the most important area for comparison is in the Makassar Strait. Figure 3 shows long-term mean $T - S$ profiles against observations in the Makassar Strait at 4.5°S , 117.5°E . This location is selected as it coincides with the core ITF flow pathway in the Makassar Strait. The mean thermohaline structure of the ITF is well captured by SODA, although the modeled salinity field is around 0.2 psu too high in the upper 100 m. This is quite likely associated with uncertainty in the surface freshwater fluxes used to force the model. Apart from this salinity offset, the vertical structure of $T - S$ in the model ITF is realistic. Comparisons at other locations, and over a full seasonal cycle, are also in reasonable agreement with the limited observations available.

The vertical structure of the ITF velocities in the Makassar Strait and within the main flow pathway through the model's Savu Strait–Timor Passage is shown in Fig. 4. The Hovmöller diagrams show depth profiles of monthly mean meridional velocity, time averaged over the 50-yr SODA reanalysis period. Apparent is the maximum in ITF rate during May–September and a minimum in December/February. This is in agreement with observed estimates (e.g., Wyrki 1987; Murray and Arief 1988) and other model simulations (e.g., Schneider and Barnett 1997; Gordon and McClean 1999). Another feature of the vertical structure of ITF flow in the Makassar Strait is the subsurface jet that appears in the upper thermocline from May to November, with peak velocities of nearly 50 cm s^{-1} in October. This is in excellent correspondence with the direct current observations of Gordon et al. (1999), although their measurements suggest a slightly deeper maximum core at $\approx 150\text{--}300$ m, compared to SODA at ≈ 100 m. Interestingly, the subsurface velocity maximum in the Makassar Strait surfaces in the Savu Strait–Timor Passage (Fig. 4b). This is consistent with observations of flow through the Timor Passage (e.g., Hautala et al. 2001), but at odds with the episodic layered flow noted in Lombok, Sumba, and Ombai Straits (Hautala et al. 2001). As noted above, however, the SODA model lacks the horizontal resolution to include these narrow ocean gateways in its bathymetry.

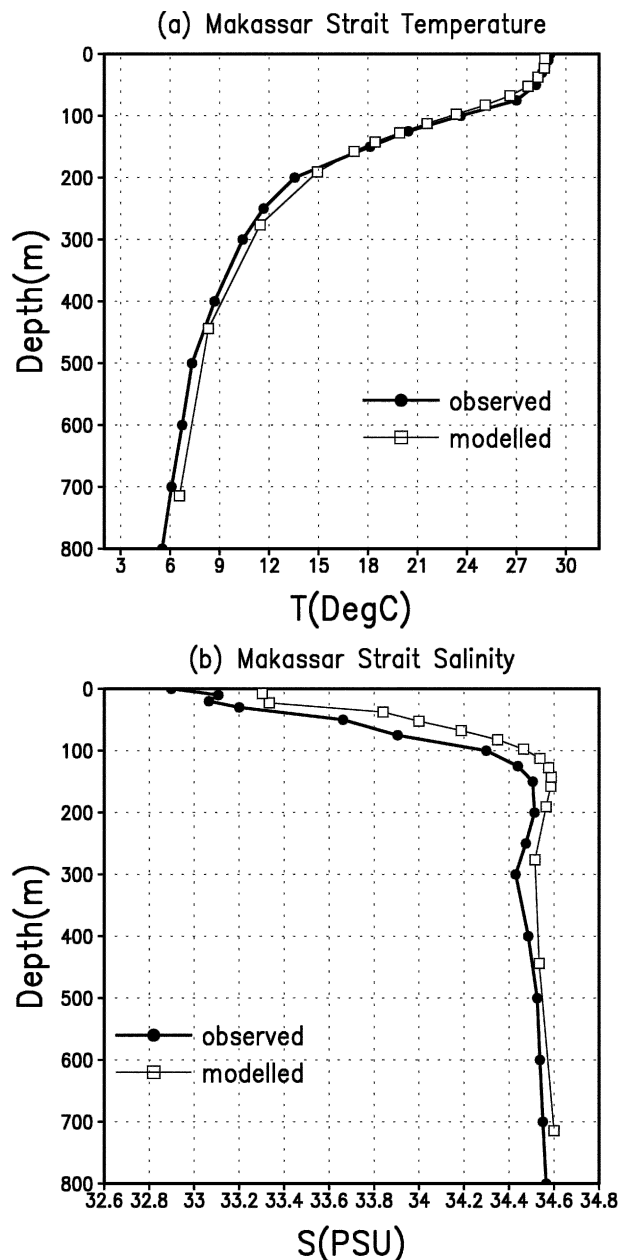


FIG. 3. Long-term mean SODA $T-S$ profiles vs observed in the Makassar Strait at 4.5°S , 117.5°E . The location is selected as it coincides with the core model ITF flow pathway in the Makassar Strait (refer to Fig. 2 for station position).

c. Validation—ITF variability

It is important to further assess the SODA model ITF simulation in terms of its interannual variability as compared to the limited observations available. Figure 1b compares the Meyers (1996) calculation of upper-ocean geostrophic transport derived from an XBT line to the equivalent quantity derived from the SODA model. As our focus is on interannual variations, the two time series are each plotted as the anomaly about

the long-term annual mean.¹ In making this comparison, we have calculated the model geostrophic flow in a manner that matches the approach adopted by Meyers (1996). In particular, we bin profiles of bimonthly model T along the same Australia–Java XBT line and combine this with a bin-averaged annual mean $T-S$ relationship to calculate dynamic height, geostrophic currents, and transport rates relative to a fixed depth of no motion. The only difference in calculation is related to the SODA grid depth levels, with the nearest depth level to the Meyers (1996) 400-dbar depth of no motion being at 444 m in the model.

The geostrophic transport time series in the model is in close phase correspondence with the observed estimate, apart from the first 12 months of the record. There are several possible reasons for this initial discrepancy in late 1983/early 1984. First, in the absence of observational data the model is freer to develop its own internal ocean circulation field. While the assimilation model incorporates all available ocean observations, few exist in the ITF region before the Meyers 1983–94 XBT line. Thus, prior to 1983 the ITF is less constrained by local T observations, and therefore more likely to respond to other modes of variability, such as those forced by the model's historical wind stress fields. Even though the observed XBT data are assimilated into the model from mid-1983 on, it is a full 12 months before the model's geostrophic flow is in phase with the observations. Another possible reason for the discrepancy early in the time series is the higher sampling error at the beginning of the Meyers (1996) record (his Fig. 2). For example, the +8 Sv anomaly in late 1983, entirely missing in the SODA model, coincides with the lowest XBT sampling density of the 12-yr record. The sparse XBT data during 1983/84 imply a larger sampling error in the observational estimates at the beginning of the record. The high positive anomaly in late 1983, for example, could in part be due to undersampling of the transect during that period.

Another part of the comparison where the model geostrophic flow in the upper 400 m differs notably from the Meyers (1996) estimate is during the 1988/89 La Niña event. During this time the model is in phase with, but underestimates, the observed upper-ocean flow across the XBT line. Possible reasons for this include: (i) the model "depth of no motion" lying well below 444 m during 1988/89, (ii) unresolved chokepoint flows via the closed Lombok and Sumba Straits, (iii)

¹ The annual mean Meyers (1996) geostrophic transport in the upper 400 m is 5 Sv compared to 9.9 Sv in the SODA model, the latter using a "depth of no motion" at the nearest model level of 444 m. This difference between the simulated and observed upper-ocean ITF transport is common among model studies. One possible cause is a model-observed mismatch in deep density fields either side of the Indonesian Passage, which will drive different throughflow rates via the joint effect of baroclinicity and relief (JEBAR).

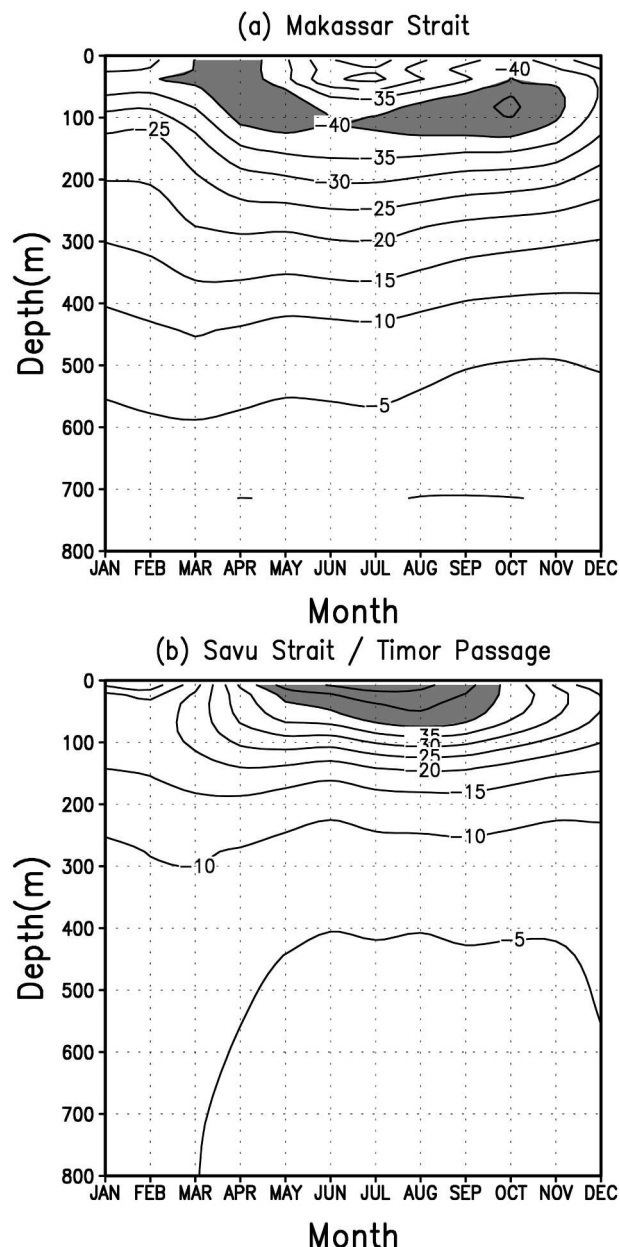


FIG. 4. Hovmöller diagrams showing seasonal and depth variations of modeled ITF flow in the (a) Makassar Strait (4.5°S , 117.5°E) and (b) in the core flow in Savu Strait–Timor Passage (10°S , 121.5°E). For station locations refer to Fig. 2. The diagrams show mean meridional velocity as a function of month, time-averaged over the 50-yr SODA reanalysis period. Contour interval is 5 cm s^{-1} . Southward flow in excess of 40 cm s^{-1} is gray shaded. The mean flow profiles are directed southward at all depths.

geostrophic flow error due to uncertainties in the SODA model's climatological wind stress forcing, and (iv) the sampling error in the observational estimate.

The upper-ocean ITF estimate from the observations of Meyers (1996) and that simulated in SODA exhibit similar magnitudes and time scales of variability: the

standard deviation of the observed ITF during May 1983–November 1994 is 3.5 Sv , compared to 2.9 Sv in the model. The two time series are also highly significantly correlated with a correlation coefficient of $r = 0.42$; well above the 99.9% confidence level ($r = 0.3$). For the most part, the SODA model captures the interannual variability of the observed ITF estimates, apart from early in the measurement record when data are sparse. Other model-derived calculations of the ITF, such as those derived directly from the simulated velocity, or calculated at other ITF chokepoints, show broadly similar behavior to that shown in Fig. 1b. The differences that appear are either due to unresolved flow below 400 m in the estimate technique of Meyers (1996), neglected ageostrophic flow such as Ekman transport, or because of short-term flow variability across sections on either side of the ITF (discussed in section 2d).

It is worth briefly considering the possible constraints placed on the model ITF behavior by the assimilation of the XBT data from 1983 onward. All tested definitions of the ITF transport rate yield only minor differences ($<0.5 \text{ Sv}$) in mean ITF before and after the assimilation of the XBT data. For example, the mean geostrophic transport in the upper 444 m of the model is 9.9 Sv during the 1983/94 XBT period, and 9.5 Sv prior to that time. The magnitude of ITF variability also appears unaffected by the XBT data; for example, the standard deviation in net transport across 8°S is changed by $<0.1 \text{ Sv}$ before and after the observational record begins. Despite this insensitivity, the assimilation of XBT data will obviously provide an additional constraint on the model ITF during 1983–94 that is missing in the first three decades of the SODA reanalyses. Prior to 1983, the model will be constrained by much sparser observations of $T - S$ in the region. The available $T - S$ fields will still influence the Pacific–Indian pressure gradients that drive the ITF. However, with sparser data, the SODA ITF will be freer to respond to other dynamical constraints, most notably those imposed by the historical wind stress fields (a combination of shipboard measurements and climatologies for the period 1950–99). It is reassuring that this does not appear to substantially change the magnitude of the model's mean ITF or its variability. In addition, a comparison of the model's large-scale tropical Pacific variability to independent observations (e.g., island tide gauge records) suggests the SODA reanalysis is for the most part well constrained in the Pacific during 1950–80 (Carton et al. 2000b), particularly for the large ENSO signals. A similar assessment cannot be made in the Indian Ocean, however, due to inadequate historical tide gauge data.

d. Definitions of ITF mass and heat transports

For the remainder of this paper we define the ITF transport as the depth-integrated velocity through a zonal chokepoint section at 8°S . We follow the convention established in Fig. 1 of positive ITF for Pacific to

Indian flow, so we change the sign of the integral. Namely, the ITF is given as

$$\text{ITF} = - \int_s \int_s v r_0 d\lambda dz, \quad (1)$$

where v is the northward velocity, $r_0 = R \cos\phi_0$ is the radius at $\phi_0 = 8.0^\circ\text{S}$ latitude, R is the radius of the earth, λ is longitude, and z is depth. The integrating area s is bounded by land, running from 120.5° to 131.5°E and from the surface down to the bottom. The mean model ITF transport is 14.5 Sv, which is toward the upper bound of observed estimates [e.g., 11 Sv, Meyers et al. (1995); 5–15 Sv, Gordon and Susanto (1999); 9.3 ± 2.5 Sv, Gordon and McClean (1999)], but typical of ocean model simulations [e.g., 17 Sv, Hirst and Godfrey (1993); 16 Sv, Schiller et al. (1998); 13.8 Sv, Schneider and Barnett (1997)].

To confirm that the calculation of ITF transport is insensitive to our choice of chokepoint location, Fig. 5 compares the 50-yr time series of depth-integrated flow southward across 8°S (the ITF as defined above) to the depth-integrated flow westward across 115°E . Over monthly time scales (Fig. 5a), the two definitions can vary by up to 2–3 Sv, indicating significant transient local mass storage in the Timor Sea and tropical eastern Indian Ocean. However, over interannual time scales (Fig. 5b), excellent correspondence is obtained between the two ITF definitions, with only 0.5-Sv discrepancies. Thus, for the purposes of this note, the analysis of interannual throughflow variability remains insensitive to our choice of ITF chokepoint location.

Other quantities analyzed in this study include SST and atmospheric properties. Sea surface temperature is taken to be the temperature in the shallowest model level. The atmospheric data used in this paper are the monthly geopotential height reanalysis data on a $2.5^\circ \times 2.5^\circ$ latitude–longitude grid, provided by the NCEP–National Center for Atmospheric Research (NCAR; Kalnay et al. 1996). Finally, heat transport associated with the ITF is calculated as

$$\text{HT} = -\rho c_p \int_s \int_s v (\theta - \theta_r) r_0 d\lambda dz, \quad (2)$$

where ρ is density (1023.0 kg m^{-3}), c_p is specific heat capacity at constant pressure ($3998.0 \text{ J } ^\circ\text{C}^{-1} \text{ kg}^{-1}$), θ is potential temperature, and θ_r is a reference temperature to take account of the necessary return flow of ITF waters south of Australia (we take $\theta_r = 3.4^\circ\text{C}$ after Vranes et al. 2002). The negative sign in Eq. (2) is taken to ensure positive values for heat transport from the Pacific into the Indian Ocean.

3. Results

a. Interannual variability of the ITF

The time series of the model ITF anomaly about the long-term mean seasonal cycle is shown in Fig. 6 (red

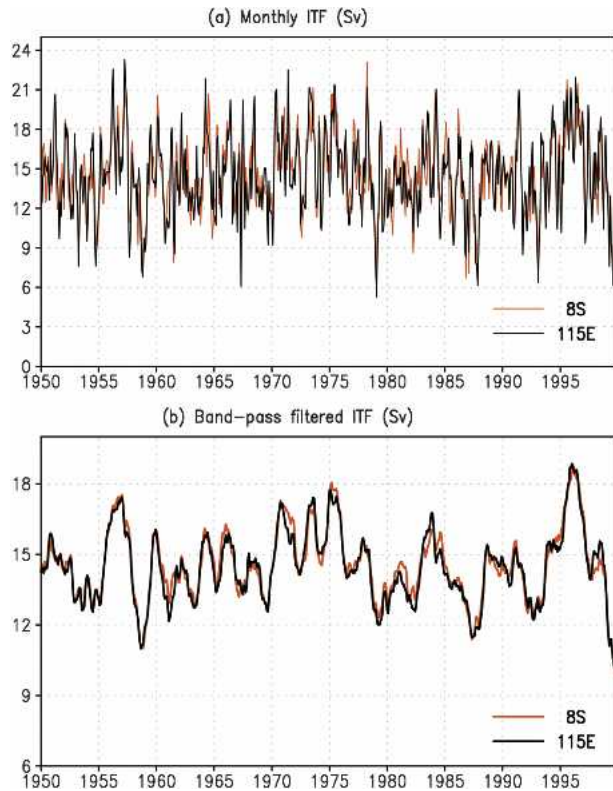


FIG. 5. Time series of (a) monthly mean and (b) 13-month running mean model ITF (Sv) depth integrated southward across 8°S and westward across 115°E .

thin line). Note that in Fig. 1 we compared the modeled and observed upper-ocean ITF geostrophic transport without removing the seasonal cycle, for direct comparison with the Meyers (1996) estimated record (solid line in his Fig. 4c). In contrast, Fig. 6 removes the seasonal cycle as well, leaving a monthly time series of anomalies about the seasonal mean, exhibiting both high- and low-frequency variability.

From the time series of ITF anomaly in Fig. 6 it is evident that there is distinct intraseasonal and interannual variability in Pacific–Indian transport beyond the seasonal cycle. To further identify the detailed characteristics of the time series in the time and frequency domain, a wavelet analysis is performed using a “Morlet” basis function. Details of this method can be found in Torrence and Compo (1998). Figure 7 shows the results from this wavelet analysis. The global power spectrum shows that the dominant period of oscillation for the ITF is about 4–7 yr (Fig. 7b). The only other significant period that passes the 95% confidence level is associated with intraseasonal variability in the 3-to-6-month band. This subannual variability of the ITF about its seasonal mean is not the focus of this paper. At the other end of the spectrum, interdecadal variability is below the 95% significance level, and best investigated using multicentury integrations of a coupled cli-

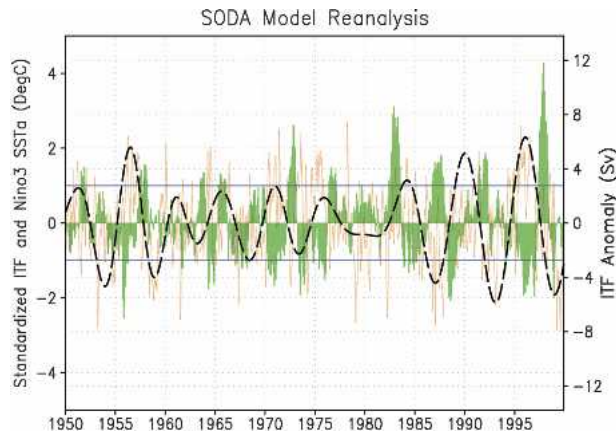


FIG. 6. Time series of the ITF transport anomaly about the long-term seasonal mean from 1950 to 1999 calculated from SODA assimilative data (thin solid red line) and its interannual (4–7 yr) band-scale time series from a wavelet analysis (thick dashed black line; for details see text). The two lines are each standardized. The green bar shows the Niño-3 SST anomaly from SODA in $^{\circ}\text{C}$. The left y-axis scale is the same for each standardized time series, and the right y axis is the ITF anomaly (Sv) corresponding to the standardized ITF line. Interannual periods of strong and weak ITF can be defined using the 4–7-yr band-scale time series (i.e., periods above +1.0 and below –1.0, respectively).

mate model. Our focus is thus on the interannual time scales. Figure 7a shows the real component of the wavelet transform coefficient for the time series of ITF in the time–frequency domain. The most obvious feature is a concentration of amplitude within the band of 2–10 yr. However, there are also frequency variations during the 50-yr record, with a split in periodicity in the mid-1960s from a broad 3–7-yr range into a mode of slightly lower frequency (with a period of about 7–10 yr) and a mode of higher frequency (with a period of less than 4 yr; Fig. 7a). The 4–7-yr band-scale average of the ITF time series (the thick dashed line in Fig. 6) is calculated as the mean of the real part of the wavelet transform coefficient (Fig. 7a) in the 4–7-yr band, and used later to define periods of strong and weak ITF (i.e., periods above +1.0 and below –1.0, respectively). This band-scale average reveals high-amplitude interannual variability during the first 10-yr of the SODA reanalysis, followed by lower-amplitude variability from the mid-1960s until about 1985, whereupon interannual variability is again high. These lower-frequency oscillations in ITF strength are, however, beyond our study, as the model record is too short to evaluate interdecadal variations with any statistical significance.

b. Linkage with tropical SST

To reveal any relationship between the interannual variation of ITF and ENSO, a composite analysis is performed on the SST fields during the periods of strong and weak ITF. We define the weak or strong ITF period as during months when the standardized inter-

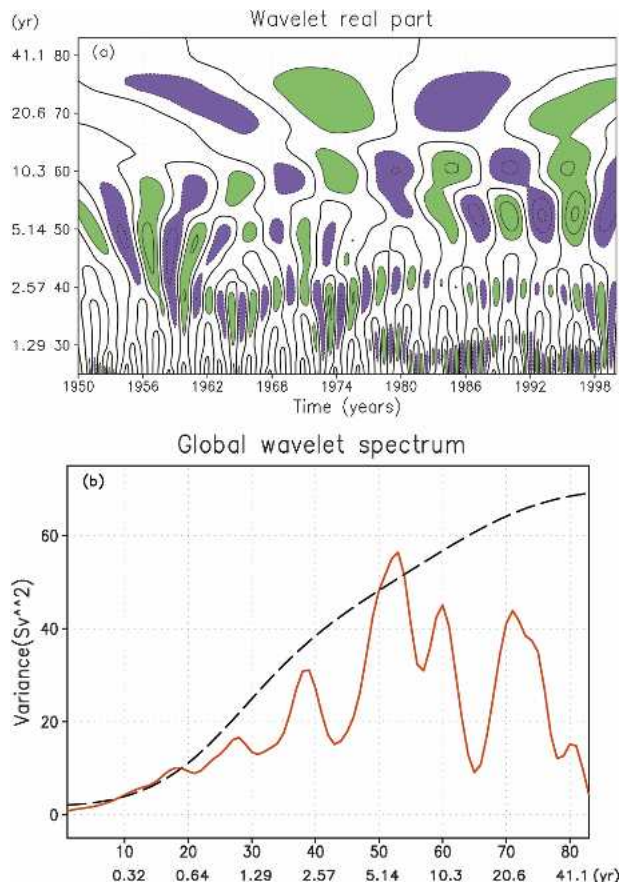


FIG. 7. Wavelet analysis of the ITF anomaly time series of Fig. 6 using a “Morlet” wavelet basis function in the time–frequency domain. (a) Real part distribution of the wavelet transform coefficient. The x axis is time (year) and the y axis is wavelet scale. The corresponding period (in years) to the scale is shown to the left of the y axis. (b) The global wavelet spectrum of ITF anomaly. The y axis is variance spectrum and the x axis is wavelet transform scale. Also shown under the x axis is the period in years corresponding to the frequency scale. The dashed line in (b) is the 95% significance level. Note that the wavelet analysis is undertaken on the ITF anomaly about the seasonal mean, which explains the low spectral energy at ≈ 1 -yr period in (b).

annual (4–7 yr) band-scale value of ITF anomaly is less than –1.0 or greater than +1.0, respectively (see the thick dashed curve in Fig. 6). Figure 8a shows the difference of the SST anomaly composite fields between strong and weak ITF periods. The most significant feature is the tropical SST anomaly showing a typical La Niña pattern over the Pacific. This confirms that there is a tendency for a larger ITF transport during La Niña periods and a smaller ITF transport during El Niño, in agreement with previous studies (e.g., Meyers 1996; Gordon and Susanto 1999). A negative SST anomaly occupies the South China Sea and most of the Indian Ocean, except for the southeast region off the west coast of Australia. This dipole distribution in the east Indian Ocean suggests that upper-ocean heat content anomalies might also play a role in ITF variability by

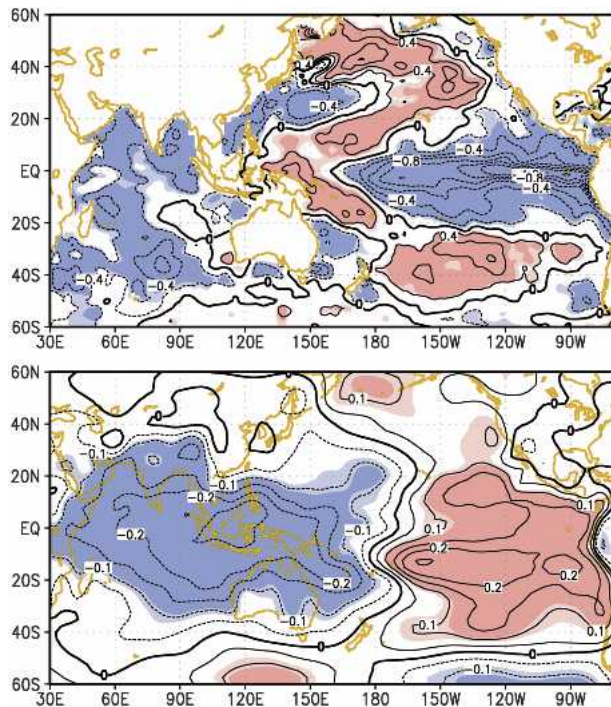


FIG. 8. (a) Difference of the SST anomaly composite fields between strong and weak ITF periods. The contour interval is 0.2°C . The thick solid line denotes zero difference. The light and heavy red (blue) shaded areas correspond to regions exceeding the 95% and 99% confidence levels using a Student t test. (b) Lag (8 month) correlation coefficient field between the interannual bandscales of ITF anomaly time series and the 1000-hPa geopotential height. The light and heavy red (blue) shaded areas correspond to regions exceeding the 95% and 99% confidence levels. The contour interval is 0.05.

controlling regional geostrophic flow in the South Equatorial Current, which is fed by the ITF. A correlation analysis also supports this finding (figure not shown). This is, however, inconclusive as Pacific-forced ITF variations can also establish heat content anomalies downstream of the Indonesian archipelago. A full model heat budget analysis would be required to determine what drives the temperature anomalies in the east Indian Ocean: local air–sea fluxes and currents, or the ITF itself.

For further analysis of the connection between ENSO and the ITF, the lag correlation coefficients between the ITF and the Niño-3 index from 1950 to 1999 are calculated. The Niño-3 index (green bar in Fig. 6) is defined as the time series of the SODA SST anomaly averaged between 5°S – 5°N , 150° – 90°W . The time series of Fig. 6 shows that the ITF is generally out of phase with the Niño-3 index. Comparing the interannual ITF time series with the Niño-3 index at zero lag, we find a negative correlation coefficient of -0.19 (exceeding the 99% confidence level). The maximum lagged correlation coefficient reaches -0.32 with the ITF lagging the Niño-3 index by 9 months (figure not shown). In sum-

mary, these results suggest that the ITF interannual variability is a lagged response to the El Niño signal in the tropical Pacific, with regional geostrophic flow in the east Indian Ocean also possibly playing a role.

c. Linkage with the Southern Oscillation

The Southern Oscillation (SO) is an atmospheric pressure fluctuation usually accompanying El Niño events. The two phenomena are combined as ENSO to indicate the coupled tropical air–sea mode of variability. Figure 8b shows the correlation coefficient field between the interannual band scale of ITF anomaly time series and the 1000-hPa geopotential height. Here the 1000-hPa geopotential height is equivalent to sea level pressure. The most prominent characteristic is a seesaw pattern with positive correlation in the east Pacific and negative correlation in the west Pacific and Indian Oceans. This is a typical Southern Oscillation pattern with the positive and negative maximum centers just south of the equator. The correlation coefficients reach their peak when the ITF variation lags the 1000-hPa geopotential height by about 8 months (figure not shown). This lag period coincides with that between the interannual variation of ITF and the Niño-3 index, suggesting that the interannual variability of ITF is mainly associated with the large-scale tropical air–sea interaction signal—ENSO.

d. ITF heat transport variability

The heat transport associated with the ITF is calculated across 8°S as in Eq. (2). The mean value of heat transport across 8°S in SODA is 0.74 PW. In comparison with recent estimates of observed heat flux in the ITF [~ 0.50 PW, Vranes et al. (2002); Talley (2003)] the SODA value is a little high, though it is weaker than that estimated in other model studies [e.g., 0.9 PW, Schneider and Barnett (1997); 1.15 PW, Schiller et al. (1998)]. One possible reason for the model-observed discrepancy is that the Vranes et al. (2002) estimate coincides with an El Niño period (December 1996–July 1998), so the ITF transport is weaker than average during their observational record.

Figure 9 shows the calculated time series of poleward heat transport (PHT) across 8°S in the SODA reconstruction. The unfiltered PHT is dominated by a seasonal cycle in upper-ocean heat content, resulting in a range from near-zero PHT up to 1.4 PW. Taking an 11-month running mean shows much lower amplitude interannual variability. Annual mean PHT across 8°S in the ITF is in the range 0.4–1.2 PW with a standard deviation of 0.21 PW. Correlation between the annual mean ITF transport rate and the annual mean poleward heat transport across 8°S is significant at the 99.9% level. This correlation comes about because PHT rates are higher during La Niña (strong ITF, warmer western Pacific) and at a minimum during El Niño (weak ITF, cooler western Pacific). In comparison with the Vranes et al. (2002) observed estimate during December 1996–

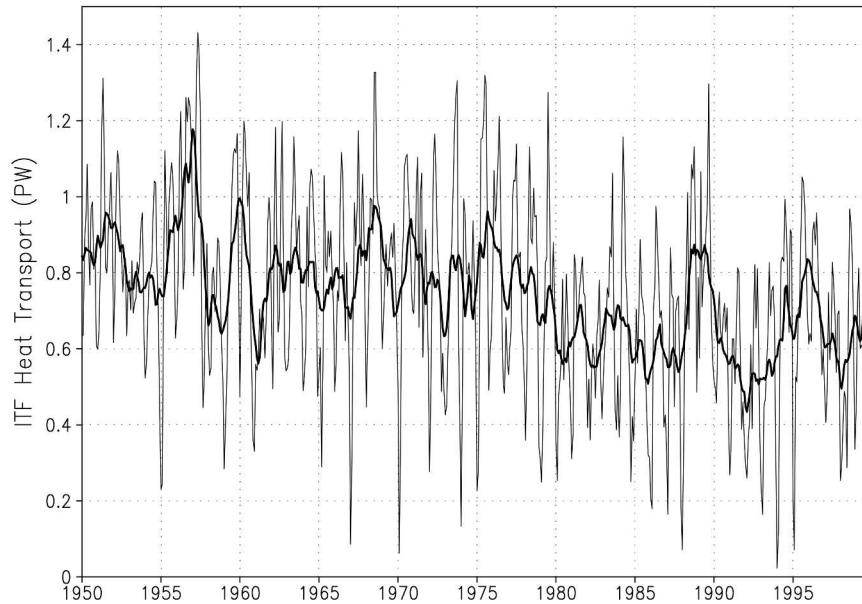


FIG. 9. The time series of poleward heat transport (PW) across 8°S from 1950 to 1999 calculated from SODA assimilative data (thin solid line) and its 11-month running mean time series (thick solid line).

July 1998 (0.50 PW), the SODA reanalysis has a mean PHT of 0.55 PW during the corresponding period. This supports the suggestion of Vranes et al. (2002) that their observed estimate is skewed slightly lower than the longer-term climatic mean.

4. Discussion and summary

We have used the relatively long time series SODA assimilative data system to examine the interannual variability of the Indonesian Throughflow and its relationship with ENSO during 1950–99. This extends the time record available in conventional observational datasets and most model reanalysis experiments. A comparison between the 1983–95 observed ITF and that simulated suggests an accurate reconstruction of ocean circulation in the vicinity of the ITF during the available measurement record. The results show that the transport from the Pacific to the Indian Ocean has a significant interannual variability with a dominant 4–7-yr period based on a wavelet analysis. Composite and correlation analyses indicate that this interannual variability is mainly linked to the El Niño–Southern Oscillation (ENSO) pattern. Lagged correlation reveals that the interannual variation of the ITF appears 9 months after the Niño-3 SST anomaly. A similar lag is found for the 1000-hPa geopotential height field from NCEP–NCAR reanalysis data, which manifests as a Southern Oscillation signal. This suggests that large-scale tropical ocean–atmosphere interactions play a dominant role in controlling the interannual variability of the ITF. In addition, regional water properties either

side of the ITF may also play a role by controlling localized geostrophic flows.

ENSO-driven variability in the ITF translates to substantial fluctuations in poleward heat transport from the Pacific to Indian Ocean. This has implications for Pacific–Indian tropical climate. In this note we examined the ITF–ENSO link in an ocean model forced by prescribed fluxes during 1950–99. There have only been a few studies of ITF transport processes in coupled climate model integrations (e.g., Schneider and Barnett 1997; Schneider 1998; Wajsowicz and Schneider 2001). Moreover, these studies either focus on variability at the seasonal time scale (Schneider and Barnett, 1997), or on the global climate difference between experiments with and without an open Indonesian Archipelago (Schneider 1998; Wajsowicz and Schneider 2001). Little analysis of variability at the interannual time scale is made, apart from that in Wajsowicz and Schneider (2001). In contrast to our study, their model does not exhibit a simple relationship between ENSO and the ITF transport rate. Importantly, they further find poor correspondence between model ITF variability and that predicted by the Godfrey (1989) Island Rule, which links the ITF to the zonally integrated wind stress curl along the latitudes limiting flow around Australia. In this note we have demonstrated a link between interannual variability in the Indonesian Throughflow and ENSO climate fluctuations in a 50-yr integration of a global ocean data assimilation experiment. Further analysis of the interannual variability of ITF and its link to ENSO should be made in full coupled climate models, so that the dynamics of the coupled teleconnection can be explored.

Acknowledgments. This research was supported by the Australian Research Council (ARC), the National Natural Science Foundation of China, the Open Research Program from the Key Laboratory of Tropical Marine Environmental Dynamics (LED), South China Sea Institute of Oceanology, Chinese Academy of Sciences, and the China Scholarship Council (CSC). The authors thank Professor J. Carton of the University of Maryland for making available the SODA model reanalysis data, and Professor Ruixin Huang of Woods Hole Oceanographic Institution for supplying the SODA model output. The constructive comments of two anonymous reviewers are also gratefully acknowledged.

REFERENCES

- Angell, J. K., 1981: Comparison of variations in atmospheric quantities with sea surface temperature variation in the equatorial eastern Pacific. *Mon. Wea. Rev.*, **109**, 230–243.
- Bray, N. A., S. Hautala, J. Chong, and J. Pariwono, 1996: Large-scale sea level, thermocline and wind variations in the Indonesian throughflow region. *J. Geophys. Res.*, **101**, 12 239–12 254.
- Carton, J. A., G. Chepurin, X. Cao, and B. S. Giese, 2000a: A simple ocean data assimilation analysis of the global upper ocean 1950–95. Part I: Methodology. *J. Phys. Oceanogr.*, **30**, 294–309.
- , —, and —, 2000b: A simple ocean data assimilation analysis of the global upper ocean 1950–95. Part II: Results. *J. Phys. Oceanogr.*, **30**, 311–326.
- England, M. H., 1993: Representing the global-scale water masses in ocean general circulation models. *J. Phys. Oceanogr.*, **23**, 1523–1552.
- Fieux, M., R. Molcard, and A. G. Ilahude, 1996: Geostrophic transport of the Pacific-Indian Oceans throughflow. *J. Geophys. Res.*, **101**, 12 421–12 432.
- Godfrey, J. S., 1989: A Sverdrup model for the depth-integrated flow for the World Ocean, allowing for island circulations. *Geophys. Astrophys. Fluid Dyn.*, **45**, 89–112.
- Gordon, A. L., 2001: Inter-ocean exchange. *Ocean Circulation and Climate*, G. Siedler, J. Church, and J. Gould, Eds., International Geophysics Series, Vol. 77, Academic Press, 303–314.
- , and R. A. Fine, 1996: Pathways of water between the Pacific and Indian oceans in the Indonesian seas. *Nature*, **379**, 146–149.
- , and J. L. McClean, 1999: Thermohaline stratification of the Indonesian Seas: Model and observations. *J. Phys. Oceanogr.*, **29**, 198–216.
- , and R. D. Susanto, 1999: Makassar Strait transport: Initial estimate based on Arlindo results. *Mar. Tech. Soc. J.*, **32**, 34–45.
- , —, and A. Ffield, 1999: Throughflow within Makassar Strait. *Geophys. Res. Lett.*, **26**, 3325–3328.
- Hautala, S. L., J. Sprintall, J. Potemra, A. G. Ilahude, J. C. Chong, W. Pandoe, and N. Bray, 2001: Velocity structure and transport of the Indonesian Throughflow in the major straits restricting flow into the Indian Ocean. *J. Geophys. Res.*, **106**, 19 527–19 546.
- Hirst, A. C., and J. S. Godfrey, 1993: The role of Indonesian Throughflow in a global ocean GCM. *J. Phys. Oceanogr.*, **23**, 1057–1086.
- Kalnay, E., and Coauthors, 1996: The NCEP/NCAR 40-Year Reanalysis Project. *Bull. Amer. Meteor. Soc.*, **77**, 437–471.
- Kindle, J. C., H. C. Hurlburt, and E. J. Metzger, 1989: On the seasonal and interannual variability of the Pacific-Indian Ocean throughflow. *Western Pacific International Meeting and Workshop on TOGA-COARE*, J. Picaut, R. Lukas, and T. Delcroix, Eds., 355–366.
- Lee, T., and Coauthors, 2002: Effects of the Indonesian Throughflow on the Pacific and Indian Oceans. *J. Phys. Oceanogr.*, **32**, 1404–1429.
- Maltrud, M. E., A. J. Semtner, and R. C. Malone, 1998: Global eddy-resolving ocean simulation driven by 1985–1995 atmospheric winds. *J. Geophys. Res.*, **103**, 30 825–30 853.
- Meyers, G., 1996: Variation of Indonesian Throughflow and El Niño-Southern Oscillation. *J. Geophys. Res.*, **101**, 12 255–12 263.
- , R. J. Bailey, and A. P. Worby, 1995: Geostrophic transport of Indonesian Throughflow. *Deep-Sea Res.*, **42**, 1163–1174.
- Murray, S. P., and D. Arief, 1988: Throughflow into the Indian Ocean through Lombok Strait, January 1985–January 1986. *Nature*, **333**, 444–447.
- Potemra, J. T., R. Lukas, and G. T. Mitchum, 1997: Large-scale estimation of transport from the Pacific to the Indian Ocean. *J. Geophys. Res.*, **102**, 27 795–27 812.
- Rasmusson, E. M., and T. H. Carpenter, 1982: Variations in tropical sea surface temperature and surface wind fields associated with the Southern Oscillation/El Niño. *Mon. Wea. Rev.*, **110**, 354–384.
- Schiller, A., J. S. Godfrey, P. C. McIntosh, G. Meyers, and S. E. Wijffels, 1998: Seasonal near-surface dynamics and thermodynamics of the Indian Ocean general circulation model. *J. Phys. Oceanogr.*, **28**, 2288–2312.
- Schneider, N., 1998: The Indonesian throughflow and the global climate system. *J. Climate*, **11**, 676–689.
- , and T. Barnett, 1997: Indonesian Throughflow in a coupled general circulation model. *J. Geophys. Res.*, **102**, 12 341–12 358.
- Schott, F. A., and J. P. McCreary, 2001: The monsoon circulation of the Indian Ocean. *Progress in Oceanography*, Vol. 51, Pergamon, 1–123.
- Talley, L. D., 2003: Shallow, intermediate, and deep overturning components of the global heat budget. *J. Phys. Oceanogr.*, **33**, 530–560.
- Torrence, C., and G. P. Compo, 1998: A practical guide to wavelet analysis. *Bull. Amer. Meteor. Soc.*, **79**, 61–78.
- Vranes, K., A. L. Gordon, and A. Ffield, 2002: The heat transport of the Indonesian Throughflow and implications for the Indian Ocean heat budget. *Deep-Sea Res.*, **49B**, 1391–1410.
- Wajsowicz, R. C., and E. K. Schneider, 2001: The Indonesian Throughflow's effect on global climate determined from the COLA Coupled Climate System. *J. Climate*, **14**, 3029–3042.
- Wolter, K., 1987: The Southern Oscillation in surface circulation and climate over the tropical Atlantic, Eastern Pacific, and Indian Oceans as captured by cluster analysis. *J. Climate Appl. Meteor.*, **26**, 540–558.
- , and M. S. Timlin, 1993: Monitoring ENSO in COADS with a seasonally adjusted principal component index. *Proc. 17th Climate Diagnostics Workshop*, Norman, OK, University of Oklahoma, 52–57.
- Wyrtki, K., 1987: Indonesian Throughflow and the associated pressure gradient. *J. Geophys. Res.*, **92**, 12 941–12 946.